Faraday Discussions

Cite this: DOI: 10.1039/d6fd00029k

PAPER

Published on 31 March 2026
Licensed under CC-BY 4.0

The non-SEI nature of the magnesium metal anode interphase in chloride-based glyme electrolytes

Sara Drvarič Talian, *[a] Jože Moškon,[a] Blaž Slabajna,[ab] Črt Saksida, [a] Olivera Lužanin,[a] Tim Šlosar,[a] Elena Tchernychova,[a] Ivan Dacrema,[ab] Nemanja Latas,[ab] Urban Košir,[ab] Gregor Kapun,[ab] Miran Gaberšček [ab] and Robert Dominko [abc]

Received 23rd February 2026, Accepted 27th March 2026

DOI: 10.1039/d6fd00029k

Magnesium metal anodes offer a promising pathway for high-energy-density post-lithium batteries, but their practical application is hindered by a poorly understood electrode–electrolyte interphase. While lithium metal anodes operate *via* an ionically conductive and electronically resistive SEI, it remains unclear if magnesium operates under similar principles. We demonstrate that the surface film formed on magnesium in chloride-based glyme electrolytes is fundamentally distinct from a traditional SEI. By combining electrochemical impedance spectroscopy with focused ion beam scanning electron microscopy (FIB-SEM), transmission electron microscopy (TEM), and X-ray photoelectron spectroscopy (XPS), we identify a dual-layer interphase consisting of a thick, porous outer layer and a thin (~10 nm), compact inner layer. Crucially, we present electrochemical and morphological evidence—including identical-location microscopy of deposits and polysulfide probe measurements—proving that this compact layer is ionically insulating but electronically conductive. Consequently, magnesium plating occurs on top of the passivation layer *via* electron tunneling, whereas stripping requires the mechanical rupture of the film. This inherent asymmetry and the "anti-SEI" nature of the magnesium interphase challenge current interface engineering strategies and suggest that future improvements must address the electronic leakage and mechanical instability of the surface film.

Introduction

Next-generation sustainable energy storage systems require anode materials that surpass the capabilities of current technologies. Research often examines

[a]*Laboratory for Modern Battery Systems, Department of Materials Chemistry, National Institute of Chemistry, Hajdrihova 19, 1000 Ljubljana, Slovenia. E-mail: sara.drvarictalian@ki.si*

[b]*Faculty of Chemistry and Chemical Technology, University of Ljubljana, Večna pot 113, 1000 Ljubljana, Slovenia*

[c]*ALISTORE – European Research Institute, CNRS FR 3104, 15 Rue Baudelocque, Amiens 80039 Cedex, France*

magnesium metal anodes, as they offer high capacity, low redox potentials, abundancy and safety. Their performance limitations are commonly attributed to an unstable and insulating Mg metal interphase, which spontaneously forms when Mg metal is placed in contact with the electrolyte and which controls the electrode's performance. Unlike the well-understood Solid Electrolyte Interphase (SEI) on lithium metal—which is ionically conductive yet electronically insulating—the nature and function of the film on Mg metal anodes remain a subject of debate.

Currently, the research often operates under the assumption that the interphase formed on Mg metal is similar to a Li SEI. As a result, studies commonly aim to improve Mg metal performance through controlling the morphology and chemical composition of its passive layer, in effect aiming to facilitate Mg^{2+} migration. The approach often involves changes in electrolyte formulation, which affects the Mg^{2+} solvation structure and directly controls the composition of the passive layer.[1,2] Another possibility is interface engineering, which employs additives[3,4] or formation of optimized artificial passivation layers.[5–7]

Nevertheless, a fundamental question on whether or not the Mg passivation layer actually permits ionic transport, or does it need to physically rupture to expose the active metal,[8,9] remains. Determining whether the interphase behaves as a true SEI or a blocking passivation film is critical, since it governs the faradaic processes, impedance losses, and overall reversibility of the anode. In this paper, we characterize the Mg metal interphase in a representative chloride-based glyme electrolyte. Although this group of electrolytes is corrosive toward current collectors and other battery components, they are compatible with electrophilic electrodes due to their non-nucleophilic nature and are commercially available, making them a good model system for studying fundamental interfacial mechanisms.

We employed electrochemical impedance spectroscopy and coupled it with advanced morphological and chemical analyses (FIB-SEM, TEM/STEM, and XPS). By proposing a dual-layer model, we explain the apparent discrepancy between electrochemical data, which suggests a thin barrier, and morphological observations of thick porous layers. Furthermore we show that the Mg interphase exhibits significant electronic conductivity while remaining ionically resistive through polysulfide experiments and identical-location microscopy. This "anti-SEI" behavior explains the observed asymmetry between stripping and plating processes and necessitates a paradigm shift in how Mg metal interfaces are modeled and engineered.

Experimental details

All electrochemical cell components were handled in an argon filled glovebox (MBRAUN), where oxygen and water content were kept below 1 ppm. Mg (100 μm thick foil, Changsha Rich Nonferrous metals, 99.95%) was brushed in eight different directions with P1200 sanding paper before electrodes were cut from it. Electrodes intended for cells with leaner electrolyte conditions (pouch cell casing, Swagelok casing) were then punched out using a round puncher. Electrodes for larger electrolyte quantity cell experiments were cut with scissors into 1 × 4 cm rectangles for the working electrode (WE) and counter electrode (CE) and a 0.5 × 5 cm rectangle for the reference electrode (RE). Electrodes for the experiment with

 This journal is © The Royal Society of Chemistry 2026

added Li_2S_8 electrolyte were round punched and pre-passivated by soaking them in a vial with the Mg-based electrolyte for 1 h before washing them with 1,3-dioxolane solvent. Li metal (Gelon, 200 µm ribbon) was used without pretreatment by punching out disc electrodes with a round puncher. Glassy carbon discs (GC, 2 cm^2, HTW) were dried at 50 °C overnight, placed in the glovebox and used as electrodes without pretreatment.

Mg electrodes intended for chemical and morphological investigation of passive layer growth were cut from 1.6 mm diameter Mg rods (Goodfellow, 99.9%) while soaking in the Mg-based electrolyte, using a cutting apparatus manufactured in-house (Fig. 1a and b). The apparatus consisted of a PEEK plastic cup with an internal diameter of approximately 2 cm and a height of 5 cm, designed to hold the electrolyte (2 mL was used). The top-down view of the cup opening was shaped like a truncated circle. A 2 mm diameter hole was drilled at a 30° inclination (from horizontal) into the cup wall on the truncated side, with the opening positioned 5 mm above the inside bottom edge of the cup. This allowed placement of a Mg rod into the electrolyte compartment (black line in the scheme) without electrolyte spillage. The cup was fixed to a manual disc puncher (MTI Corporation), which was placed inside the glovebox and modified by replacing the puncher with a guillotine-like blade capable of cutting the Mg rod inside the electrolyte

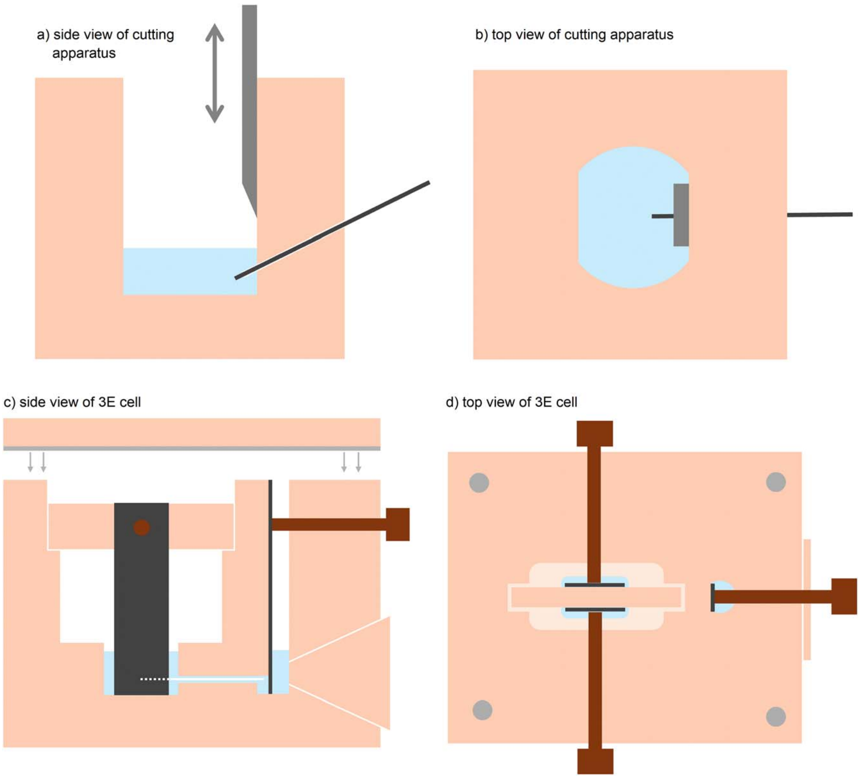

Fig. 1 Schematics of the Mg rod cutting apparatus in (a) side view and (b) top view. Schematics of the 3E cell in (c) side view and (d) top view.

compartment. To ensure a cleaner cut, the blade was plunged into the apparatus alongside the inside truncated edge of the cup.

The Mg-based electrolyte in all experiments was 0.4 M $MgCl_2$, 0.4 M magnesium bis(trifluoromethanesulfonyl)imide ($MgTFSI_2$) in tetraglyme (TEGDME) : 1,3-dioxolane (DOL) 1 : 1 (v/v) solvent mixture. All components were dried before use: $MgTFSI_2$ (Solvionic, 99.5) was dried overnight under vacuum at 220 °C, $MgCl_2$ (Thermo Fisher Scientific, 99.99) was used as received, TEGDME (99%, Acros) and DOL (Sigma-Aldrich, HPLC grade, 99.9%) solvents were dried using 4 Å molecular sieves for five days, refluxed overnight with a Na/K alloy, and subsequently purified by fractional distillation. All procedures were done inside the glovebox to prevent contamination with water. The final water content was determined by Karl Fischer titration (Mettler Toledo, C20) and confirmed to be below 1 ppm. The electrolyte was prepared in the glovebox in a volumetric flask by first dissolving $MgTFSI_2$ in the solvent mixture. Then $MgCl_2$ was added and dissolved, until finally the solvent mixture was added to the volumetric marking on the flask.

Li_2S_8 powder used for preparation of the polysulfide solution was synthesized by mixing stoichiometric amounts of Li and sulfur (Sigma-Aldrich, 99.98%) in tetrahydrofuran (Sigma-Aldrich, 99.9%), heating the mixture to 50 °C until the reactants dissolved, and isolating the product under reduced pressure inside the glovebox. 100 mM Li_2S_8 solution in TEGDME : DOL 1 : 1 (v/v) mixture was prepared analogously to the Mg electrolyte in a volumetric flask inside the glovebox. Since polysulfides tend to disproportionate, the concentration of this catholyte solution should be considered nominal. For the *operando* polysulfide addition experiment, 0.5 M polysulfide solution was prepared in the same solvent mixture.

Symmetrical lean-electrolyte Mg||Mg cells were assembled by placing a 13 mm in diameter glass fiber (GF-A, Whatman, 260 μm) separator between the two brushed Mg electrodes 12 mm in diameter and wetting it with 80 μL of the Mg electrolyte. The stack was sealed inside a Swagelok type cell with graphite discs (Ted Pella, Carbon Planchets 10 mm) between Swagelok cell stainless steel current collector rods and the Mg electrodes in order to minimize corrosion of the casing by the chloride containing electrolyte. Symmetrical Li||Li cells were assembled by placing an 18 mm in diameter Celgard 2320 separator between two Li electrodes 16 mm in diameter and wetting it with 20 μL of 1 M $LiPF_6$ in ethylene carbonate (EC) : diethyl carbonate (DEC) 1 : 1 (v/v) electrolyte (LP40, Elyte). The stack was placed inside a pre-fabricated and dried triplex (PE 90 μm/Al 10 μm/PET 20 μm) pouch casing with Ni current collectors and heat sealed inside the glovebox. Stack pressure was ensured by an external clip placed on the pouch cell, which maintained approximately 150 kPa of pressure. Cells with polysulfide-based electrolyte were assembled with the use of pre-soaked Mg electrodes or GC electrodes and glass fiber separators with the same procedure as Li metal electrodes – by placing them in triplex pouch casing and heat sealing it.

For the flooded three-electrode cell configuration, an in-house cell from polypropylene (PP) plastic was used (Fig. 1c and d). The cell contains two compartments, one for WE and CE (left in scheme) and one for RE (right in scheme) connected *via* an electrolyte bridge in the form of a glass fiber protruding into both compartments near the inside bottom edges of the compartments (white line in Fig. 1c). The WE and CE are placed parallel to each other and parallel to the fiber placed in their middle in a 4 × 15 mm electrolyte compartment. The WE and CE electrode strips are kept 4 mm apart by a PP separator block placed above the electrolyte compartment. The WE and CE are fixed to the separator block with flat end screws from the sides of the cell, which also serve as current collectors. The WE/CE compartment holds 0.7 mL of the electrolyte. The RE compartment is narrower (5 mm diameter). The RE is contacted by a flat end screw fixing the Mg strip into the body of the cell perpendicular to the WE and CE contact screws. The glass fiber bridge can be extracted for cleaning or replacement by unscrewing a cap from the bottom side next to the RE compartment. The cell can be sealed from the top with a lid, a gasket and four screws and taken outside the glovebox for short measurements, but we have not tested its sealing durability against longer periods of atmosphere exposure.

Impedance spectra of the examined symmetrical cells were measured at OCV with a VMP-3e Bio-logic potentiostat/galvanostat. 5 mV (rms) amplitude and 1 MHz–20 mHz frequency range were employed, except in the *operando* experiment, where we limited the frequency range to 1 MHz–100 mHz. Impedance spectra were processed in Zview®, version 4 by fitting the higher frequency region of the visible arc (region with fewer distortions) with an arbitrary R_{el}–R (CPE) circuit in order to extract the changes in the arc resistance (R) and capacitance (C) values. The latter were calculated from the obtained CPE-P (here denoted as P) and CPE-T (denoted as T) parameters using eqn (1).

$$C = R^{\frac{1-P}{P}} T^{\frac{1}{P}} \tag{1}$$

Before chemical or morphological analysis of the Mg electrode samples, the electrodes were washed with DOL and dried before using vacuum-transfer holders to transfer them from the glovebox to the intended instrument.

Surface morphology of the electrodes cycled at different currents was examined using a SUPRA 35VP (Zeiss, Germany) scanning electron microscope. The acceleration voltage for SEM imaging was set to 1.0 kV. For identical location scanning electron microscopy a HR-SEM Apreo 2S (Thermo Fisher Scientific) was employed. Micrographs were measured at an accelerating voltage of 2.0 kV and a beam current of 25 pA *via* an Everhart–Thornley detector (ETD). To maintain inert conditions, all samples were transferred from the Ar-filled glovebox to the microscope vacuum chamber (and back) using a CleanConnect Sample Transfer System. The Mg foil substrate was initially rinsed with DOL inside an Ar-filled glovebox to remove bulk electrolyte. After transferring to the SEM, micrographs of different deposits were recorded to enable direct comparison with the same locations after the deposits were subsequently removed. The sample was returned to the Ar-filled glovebox for localized deposit removal. Selected Mg deposits were mechanically delaminated from the substrate using a polyethylene (PE) wedge as a scraping tool. The sample was then re-transferred to the SEM to characterize the morphology and elemental composition of the newly exposed sites. A washing procedure was performed to remove the electrolyte salt residues that were found after the deposits were removed. A glass pipette was used to apply a single drop of DOL directly onto the regions of interest on the sample still remaining on the SEM holder. The solvent was allowed to evaporate (30 seconds), and this micro-washing cycle was repeated five times per site. Final HR-SEM imaging was then performed.

FIB cross-sectional analysis was performed using a FIB-SEM Helios G5 UC equipped with a multi-gas injection system (GIS), a CleanConnect sample transfer system (Thermo Fisher Scientific, The Netherlands) and Ultim max 65 EDX detector (Oxford, UK). Samples and the FIB lift-out grid were mounted into a CleanConnect capsule inside an Ar-filled glovebox and transferred in Ar 5.0 overpressure (200 mbar) directly to the FIB instrument. The sample surface was initially protected by a 500 nm Pt layer using electron beam induced deposition (EBID, 2 kV at 0.4 nA). Subsequently, an additional Pt layer was deposited using Ga^+ ion beam induced deposition (IBID, 30 kV at 0.23 nA) to achieve a protective layer with a final thickness of 1.8 μm. Morphological images of the cross sections were recorded using a low energy electron beam (1 kV @ 50 pA) by using standard ETD and ICE detectors. Detailed information at the SEI region was acquired using an InColumn integrated TLD detector and a pre-monochromated electron beam at 500 V energy and 6.3 pA beam current.

TEM lamella was prepared by first thinning the sample to 250 nm thickness using FIB at 30 kV by sequentially reducing ion beam currents from 780 pA to 80 pA due to sample sensitivity. Subsequently, the lamella was carefully thinned to 100 nm using FIB at 16 kV with a 24 pA beam current. Afterwards, the lamella was sequentially polished on both sides using FIB at 5 kV at 44 pA, 2 kV at 25 pA, and 1 kV at 20 pA until electron transparency (∼80 nm) was achieved. The prepared lamella sample was transferred with a vacuum transfer system directly from the FIB chamber to the glovebox, where it was mounted to the TEM vacuum transfer holder.

X-ray photoelectron spectroscopy (XPS) measurements were carried out using a Versaprobe 3 AD (Phi, Chanhassen, USA) system equipped with a monochromatic Al-Kα1 excitation source (1486.7 eV). Spectra were collected using a 200 μm spot size with the charge neutralizer enabled, as the Mg rods were mounted on non-conductive double-sided Scotch tape. High-resolution spectra were recorded at a pass energy of 27 eV and a step size of 0.05 eV. Depth profiling was conducted by sputtering a 1×1 mm^2 area using 2 kV Ar^+ ions at a chamber pressure of approximately 2×10^{-7} Pa for a total duration of 80 minutes, in intervals of 3×0.1, 0.2, 0.5, 3×1, 2×2, 3×4, and 12×5 seconds. The energy scale was corrected by setting the C 1s peak of adventitious carbon to 248.8 eV. Data analysis was done using MultiPak.

The samples prepared for scanning transmission electron microscopy (STEM) using FIB were transferred from the glovebox to the microscope using a vacuum-transfer TEM holder (Gatan, USA). STEM analyses were carried out on a probe Cs-corrected JEOL ARM-200CF operated at an accelerating voltage of 80 kV to minimize beam damage. During these analyses, high-angle annular dark-field (HAADF) and annular bright-field (ABF) detectors were used simultaneously with collection semi-angles of 95–370 mrad and 10–24 mrad, respectively.

Results

When the impedance of a magnesium metal electrode is characterized at open-circuit voltage (OCV), the spectra typically display a slightly deformed arc that increases in resistance, while its peak frequency decreases. If the time evolution of the data is plotted, the resistance increases almost linearly, the capacitance remains nearly constant, and the peak frequency decreases inversely with time

 This journal is © The Royal Society of Chemistry 2026

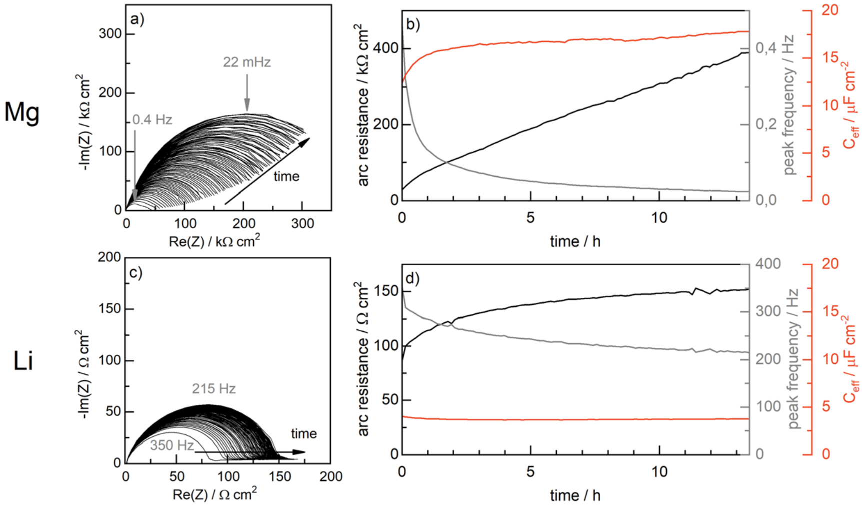

Fig. 2 EIS spectra of (a) Mg metal symmetrical cell at OCV and (b) changes to the resistance, capacitance and peak frequency over the first 13 hours of the experiment. (c) EIS spectra of Li metal symmetrical cell at OCV and (d) changes to the resistance, capacitance and peak frequency over the first 13 hours of the experiment.

(Fig. 2a and b). To begin understanding this impedance response, it is instructive to compare it to a more well-known metallic anode: lithium metal. The impedance response of a lithium metal electrode is usually explained by attributing the large high-frequency arc at intermediate frequencies to the resistance from Li^+ ion migration through the compact solid electrolyte interphase (SEI) layer on the electrode. There are additional, smaller contributions at lower frequencies, corresponding to diffusion in the porous SEI and porous separator layers[10] (Fig. 2c).

Let us now compare the response of Li and Mg electrodes. Both show the same direction of changes for resistance and peak frequency, except that in the Li metal electrode case, the arc resistance growth levels out (Fig. 2d). In the measured time frame, the resistance of the high frequency arc in the Li metal EIS spectrum increases ×2, while in the Mg case, the resistance increases ×10. Importantly, the absolute value of the resistance is about 1000× lower in the Li metal case: 75 to 150 Ω cm^2 in Li *vs.* 40 to 400 kΩ cm^2 in Mg. If the experiment with Mg is continued, the resistance increases to over 1 MΩ cm^2 in 72 h.

Since the charge transfer reaction is considered negligible on Li metal, the drift in the resistance of the high-frequency arc for Li electrodes is usually attributed to changes in the transport properties of the SEI; that is, the SEI gradually becomes more ordered, denser, or less defective, which decreases its specific ionic conductivity for Li^+ ions.[11] Importantly, the resistance growth cannot be associated with changes in SEI thickness, since the capacitance remains constant with an approximate value of 4 µF cm^{-2}. As this capacitance is directly correlated with the dielectric properties of the region occupied by SEI, its constant value indicates very strongly that the volume (and thus thickness) of this region remains constant over time.

When trying to understand the measured EIS changes in Mg metal anodes, one must first consider that unlike in lithium, the charge transfer reaction for this system is not negligible.[12] The response is therefore always a combination of the passive film resistance and the charge transfer reaction resistance, with the possibility that one is significantly larger and dominates the other.

Since the capacitance value remains similar (17 μF cm^2), we assume, as in the case of lithium, that there are no significant geometrical changes associated with the phenomena observed in the spectra; that is, neither the thickness of the probed passive layer nor the surface area associated with double layer formation at the electrode changes. One possibility is that the measured response is dominated by the charge transfer reaction resistance, which increases due to a decreasing number of available reaction sites as a consequence of passive film evolution. Alternatively, the passive film resistance and charge transfer reaction resistance may be of similar importance, with the impedance spectra drift originating from both phenomena. Third, if we mirror the Li case, one possibility for the observed drift is that the charge transfer reaction resistance is significantly smaller than the passive layer resistance, and the resistance growth is due to the passive film reordering and becoming less conductive as the number of defects decreases.

If we assume that the measured capacitance originates from the passive film properties, we can estimate its thickness. Assuming a dielectric constant of 10 for the surface film, this would suggest a 0.5 nm thick passive layer in the magnesium case and a 2 nm thick layer in the Li case. To determine the actual thickness of the passive film on Mg metal as well as its chemical composition and morphology, we conducted passivation experiments on Mg electrodes, which were cut inside the electrolyte and left to passivate for 1 h *vs.* for 72 h. In this extended time frame, the resistance increased by a factor of 25, while the capacitance of the passive layer increased by a factor of 2.4 (15 to 36 μF cm^{-2}).

The surface of the Mg sample soaked for 1 h shows a few pores at the top of the electrode, (black arrows pointing to white spots, Fig. 3a), while an approximately 300 nm thick porous layer is evident on the sample soaked for 72 h (Fig. 3b), suggesting a significantly different passive layer thickness. Furthermore, in the 72 h sample, the topmost 3 μm of bulk magnesium shows a changed structure with no visible grain boundaries. The high resolution Mg 2p XPS spectrum of the 1 h soaked sample shows the presence of peaks attributed to elemental Mg^0 (Fig. 3d), while for the 72 h sample no Mg^0 is evident (Fig. 3f), supporting the FIB-SEM analysis and suggesting growth of the passive layer thickness. The O 1s XPS spectrum shows the presence of MgO and organic oxygen compounds in the 1 h sample (Fig. 3c), while in the 72 h sample, no MgO is evident and additional changes in organic oxygen compounds are detected.

The samples were further examined through XPS depth profiling, which confirmed that the layer in the 1 h sample is thinner compared to the 72 h sample (Fig. 3h and j). Namely, the sputtering depth required until Mg^0 is detected (peak at approximately 49 eV and plasmon signal 12 eV higher) is significantly smaller for the 1 h sample than for the 72 h sample. Note that we have a residual O 1s spectra signal that never decreases in both samples (Fig. 3g and i), the origin of which is unclear. This could be due to oxygen present in the sample, degradation from the sputtering procedure, or re-passivation by residual oxidizing compounds in the XPS chamber.[13] The final oxygen and magnesium peak positions differ

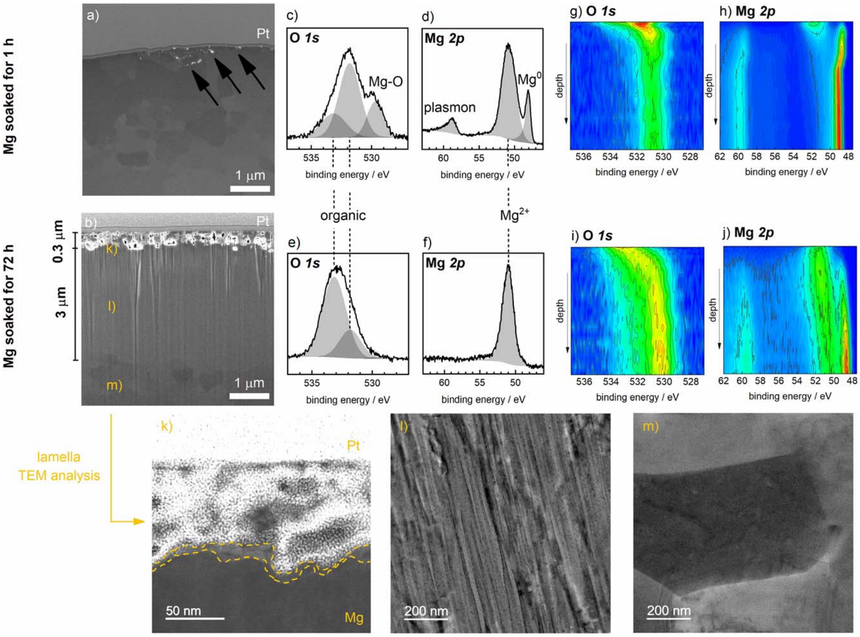

Fig. 3 Morphological and chemical composition of the passivation layer on Mg metal: (a) FIB-SEM cross section of the Mg electrode soaked in the electrolyte for 1 h, (b) FIB-SEM cross section of the Mg electrode soaked in the electrolyte for 72 h, (c) and (d) O 1s and Mg 2p XPS spectra of the Mg electrode surface after 1 h soaking, respectively, (e) and (f) O 1s and Mg 2p XPS spectra of the Mg electrode surface after 72 h soaking, respectively, (g) and (h) O 1s and Mg 2p XPS spectra during sputtering of the Mg electrode surface after 1 h soaking, respectively, (i) and (j) O 1s and Mg 2p XPS spectra during sputtering of the Mg electrode surface after 72 h soaking, respectively, (k) HAADF-STEM image of the topmost region of the FIB-prepared lamella from the 72 h sample, showing a porous surface layer heavily influenced by Pt deposition, and a denser subsurface layer (yellow dashed line), TEM micrographs of the (l) middle region of the lamella, and (m) bottom region of the lamella.

between the 1 h and 72 h samples (530.7 eV *vs.* 530.2 eV and 49.1 eV *vs.* 48.6 eV), but their binding energies are the same relative to each other. We propose that the oxygen peak arises from the same chemical species, while the position differs due to the identical calibration procedure used for samples with significantly different passive layer thicknesses. Namely, the spectra were calibrated to the adventitious carbon peak, which is a surface species. Since we expect the passive layer to be a poor electronic conductor, a gradient in the electrostatic potential with depth is likely affecting the binding energy of the species located at deeper levels, shifting their binding energy positions.

At first glance, this analysis reveals a very pronounced discrepancy between the EIS data and the FIB-SEM/XPS analysis. The former suggest a passivation layer on the order of a nanometer, while the FIB-SEM/XPS results indicate much thicker, porous and heterogeneous structures that differ significantly between the two examined samples in morphology, thickness and chemical composition. To explain this apparent mismatch, we propose a model similar to Li metal passivation: a thin, compact passivation layer directly in contact with the metal and a thicker, porous passivation layer on top.[10] The two layers differ in their preferential modes of transport. Due to the open structure of the upper layer, transport occurs through migration and diffusion in the liquid electrolyte trapped in the pores of the passivation layer. The compact passivation layer beneath this porous one, however, requires solid-state conduction. For Li metal, the conductivity of this layer for Li^+ ions is high (*i.e.*, it is an SEI), while the compact passivation layer on Mg metal does not allow Mg^{2+} migration through it (*i.e.*, it is not an SEI), resulting in significantly larger associated resistances.

To further characterize the passivation layer and visualize its thickness, the 72 h sample was processed using FIB-SEM to produce an electron-transparent lamella, which was then examined by transmission electron microscopy (TEM/STEM). For lamella preparation, we intentionally selected a region on the electrode with a thinner porous surface layer to produce a more stable lamella that would not decompose during handling or transfer between instruments. Three different points on the lamella were examined with TEM/STEM, as labeled in Fig. 3b. The top part of the lamella corresponds to the porous surface layer previously observed by FIB-SEM. This region appeared significantly affected by protective Pt deposition applied during FIB-SEM preparation, as indicated by its increased brightness (with brightness being roughly proportional to the square of the atomic number) in HAADF-STEM imaging (Fig. 3k). Notably, directly beneath this Pt-affected porous layer, a denser and more uniform layer with a thickness of approximately 7–10 nm was observed (Fig. 3k, yellow dashed lines). We interpret this feature as the compact passivation layer probed by EIS. The thickness of this layer and the capacitance obtained from EIS suggest that its dielectric constant is in the range of 4.8–6.9, a reasonable value for layers of similar composition, especially when defects are considered (noting that MgO has a permittivity around 10). The bottom layer showed crystalline Mg with a grain size of approximately 0.5 μm in diameter (Fig. 3m), while the middle layer exhibited a mixture of amorphous and crystalline Mg (Fig. 3l). We attribute this change to the consumption of Mg metal during surface passivation layer formation.

Although we took care to minimize the effects of sample handling during *ex situ* analysis, we acknowledge that the procedure might have affected the interfaces we attempted to characterize. An example of such interference was discussed in the XPS depth-profiling experiment, where residual oxygen species were present regardless of sputter time. Although *operando* analysis would improve the validity of the results, it often requires special setups or even synchrotron use.[14,15] Therefore, our approach is to emphasize the differences between the two samples (1 h *vs.* 72 h), which were handled identically. The most significant differences are the presence of a several hundred nanometer thick porous layer on the 72 h sample and the absence of inorganic species on its surface. Combined with the EIS analysis, these differences suggest that Mg metal forms a dual passivation layer in the examined electrolyte, consisting of a thin, compact passive layer (up to 10 nm thick) directly on the surface of the bulk Mg metal, and a porous, open passive layer (up to several hundred nanometers thick, depending on the electrode's contact time with the electrolyte) on top of the compact layer. From top to bottom, the passive layer becomes less organic and more inorganic in nature. In impedance measurements, only the compact layer is detected, as it is poorly conductive and exhibits high resistance. In contrast, the

 This journal is © The Royal Society of Chemistry 2026

porous passivation layer permits mass/charge transport through the electrolyte within its pores, so its resistance is likely small and insignificant.

After examining the electrodes at OCV, the next question is what happens when current is applied. This was studied using a three-electrode cell with excess electrolyte, where WE, CE and RE were all Mg foil strips. The reference electrode compartment was physically separate from the WE and CE compartment, but was connected to it by an electrolyte bridge with a glass fiber connection. The electrodes were polarized at different current densities (10, 3, 1, and 0.3 mA cm^{-2}), with the total capacity kept constant by varying the time of the experiment. The experiment revealed an asymmetry in the response between the stripped and plated sides (Fig. 4a). Specifically, after a certain period, the overpotential on the stripped electrode side abruptly drops by more than tenfold (from 500 mV to 40 mV, then decreases further). This abrupt drop in overpotential has been observed multiple times during cycling of Mg metal batteries and is attributed to activation of the electrode through mechanical breakage of the non-conductive passivation layer.[16–19]

If the current density is varied, the time at which this activation occurs remains roughly constant (between 0.5 and 1.5 h). This means that more charge passes at higher current densities before the electrode is activated (*i.e.*, the drop in overpotential in Fig. 4b occurs at higher capacities for higher currents). The overpotential before activation does not show a clear correlation with the applied current. It is generally higher for larger currents, but does not scale directly with

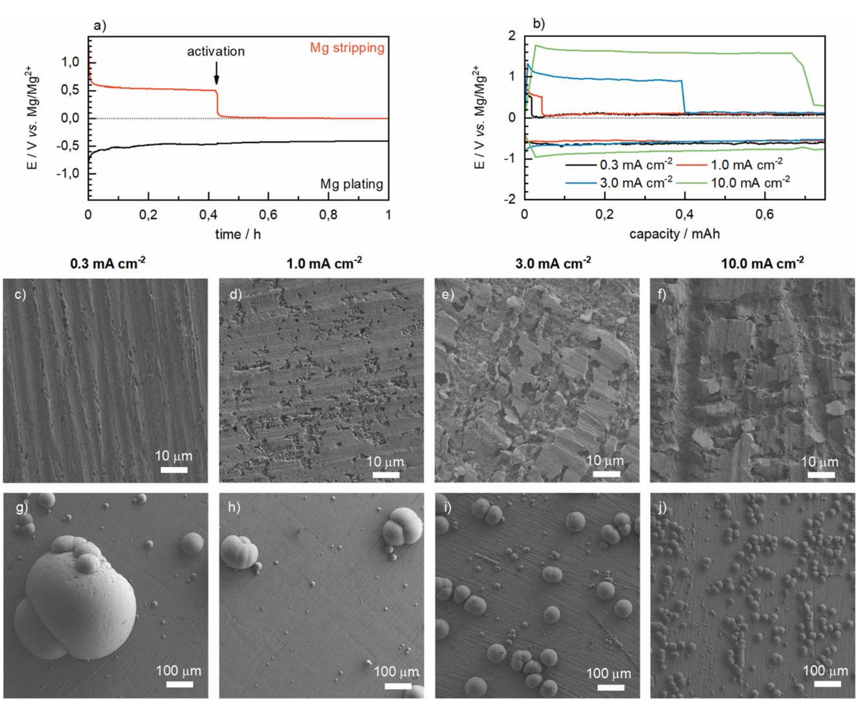

Fig. 4 (a) Overpotentials during stripping and plating (b) at various current densities and SEM micrographs for the stripped electrode (c–f) and plated electrode (g–j) at the tested current densities.

the difference. After activation, when the overpotentials are significantly lower, variation with current is more pronounced: 94 ± 6 mV, 84 ± 30 mV, 150 ± 30 mV, and 310 ± 10 mV for 0.3, 1.0, 3.0, and 10.0 mA cm^{-2}, respectively (measured in at least three repetitions for each current). Nevertheless, we are not comfortable drawing direct conclusions from these values, since the reference electrode used was Mg metal, which we do not consider stable or reliable enough to detect differences on the order of 10 mV between different cells.

SEM analysis of the electrodes shows an increasing percentage of the surface covered with pits as the current increases (Fig. 4c–f). Since the amount of Mg removed from the electrode was kept constant in all experiments, this suggests the presence of a porous network of missing Mg beneath the apparent surface, with few pits in the topmost layer (Fig. 4c). SEM micrographs of the plated electrode at the tested current densities show a decrease in the size of the deposits and an increase in the density of the coverage as the current increases (Fig. 4g–j), an effect well known from the theory of electrodeposition.

Interestingly, none of the plated electrode surfaces show any breakage in the passivation layer, with lines from mechanical brushing during electrode preparation still visible. This aligns with the observation that the plated electrode does not exhibit the same activation behavior as the stripped electrode (Fig. 4a). Additionally, the overpotentials at different currents show minimal variation during plating, with 0.3, 1.0, and 3.0 mA cm^{-2} current densities all resulting in approximately 550 mV overpotential. At 10 mA cm^{-2}, a larger difference (800 mV, Fig. 4b) is observed, but this is still far less than the several-fold difference that would mimic the current change.

This raises the question of the underlying mechanism of deposition. Since electrochemical experiments provide no evidence of electrode activation and SEM analysis indicates an intact passivation layer at the examined size scale, we suggest that Mg deposition may occur while maintaining the passivation layer intact. We hypothesize that this is possible through relatively fast electronic transport through the passivation layer, particularly under voltage bias. Such transport can occur *via* electron tunneling, which is significantly enhanced under voltage bias (following a cubic law), as known from the literature (Simmons model).[20] Thus, for Mg deposition to occur, the electron can tunnel from the metal side through the passivation layer and react with Mg^{2+} ions in the electrolyte, resulting in the deposition of a new metal layer on top of the passive film. This mechanism is straightforward, preserving the original state of the passivation layer and eliminating the need for electrode activation. In contrast, the mechanism during stripping must be very different, as this process requires Mg^{2+} ions to form below the passive film and then pass through the region occupied by the passive film. Since the film is ionically non-conductive, this passage can only occur if the passivation layer breaks, which is usually observed in galvanostatic experiments as the activation of the electrode immediately (soon) after imposing a galvanostatic step to the OCV conditions.

One aim of this contribution was to support the hypothesis that the passivation layer on Mg is electronically conductive. To address this, we conducted two different experiments: one electrochemical and one morphological. Since we assume that deposits form on top of the passivation layer created under OCV conditions, this implies that (i) the deposits are relatively weakly bound to the electrode surface and (ii) there is no "stem" connecting the deposit to the bulk

Mg. To test this, we used an electrode onto which Mg was deposited in relatively large, visually observable deposits, spaced far enough apart to allow selective mechanical removal of some deposits (Fig. 5a; the arrow indicates the removed deposit). The electrode was examined by SEM before being returned to the glovebox, where some deposits were carefully scraped off without damaging the electrode surface. The sample was then washed again to remove any electrolyte salt trapped underneath, in order to check whether a "stem" was present.

As shown in the SEM micrograph of the deposit before removal, the electrode surface displayed a morphology similar to that observed in the previous experiment where the current density was varied (Fig. 4g–j). The area around the deposit was smooth and free of cracks, with visible indentations caused by brushing the Mg surface with sandpaper during electrode preparation. The selected deposit was round, with a total diameter of 0.5 mm, and consisted of several merged grains (Fig. 5b). After the deposit was removed, the electrode surface underneath showed no evidence of a connection between the bulk electrode and the removed deposit, nor any breakage in the passivation layer (Fig. 5c). We also found some of

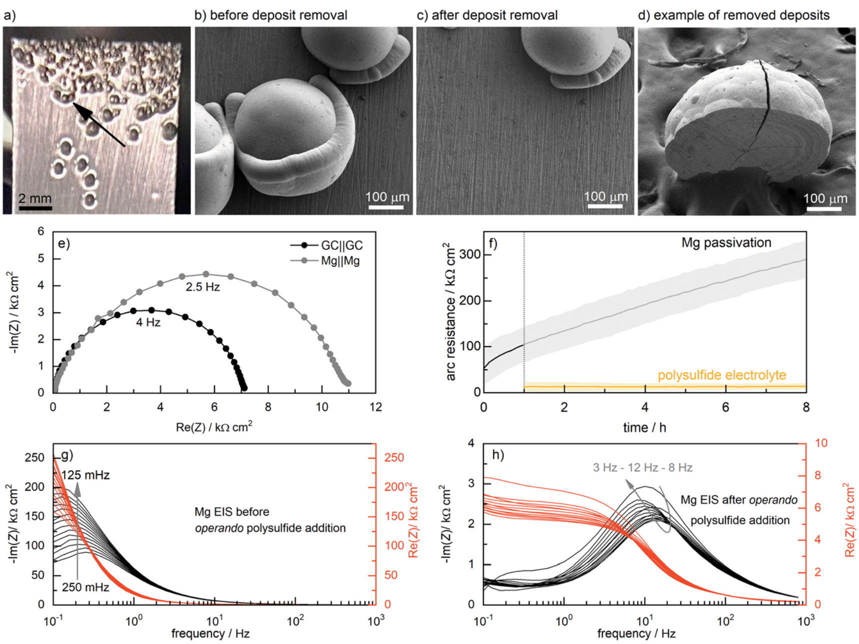

Fig. 5 Identical location microscopy on a sample of a magnesium metal electrode with large electrochemical deposits. (a) Shows a photograph of the sample with the arrow pointing to the deposit examined with the microscope, SEM micrographs (b) before, (c) after deposit removal, and of (d) example of removed deposits. (e) EIS spectra of 100 mM Li_2S_8 in TEGDME : DOL 1 : 1 (v/v) solution in symmetrical GC||GC or Mg||Mg cell, (f) comparison of the high frequency arc resistance growth in Mg||Mg cell during passivation at OCV with a Mg^{2+} electrolyte (black/grey line with the shaded area showing standard deviation) and in a Mg||Mg cell after 1 h vial passivation and subsequent cell assembly with 100 mM Li_2S_8 in TEGDME : DOL 1 : 1 (v/v) (yellow line with the shaded area showing standard deviation), (g) Bode plots of impedance spectra of Mg electrode before *operando* polysulfide addition (1 h of passivation) and (h) Bode plots of impedance spectra of Mg electrode after *operando* polysulfide addition (1 h of stabilization).

the removed deposits produced during sample handling on the surrounding carbon tape on the SEM stage. Micrographs of their bottom surfaces mirrored the Mg brushing marks and further support the hypothesis that Mg is deposited on top of a stable passivation layer (Fig. 5d). We assume cracking of the deposit happened due to either washing or physical removal of the deposits.

Additionally, we attempted to demonstrate that the passivation layer exhibits electronic conductivity by measuring the electrochemical impedance response of a symmetrical Mg||Mg cell with a polysulfide-containing electrolyte. Lithium polysulfides have been extensively studied as intermediate electroactive compounds in Li–S batteries. They readily dissolve in several ether-based electrolytes, with the catholyte typically containing various polysulfide oxidation states due to their tendency to disproportionate and comproportionate. When polysulfide species are added to a planar glassy carbon symmetrical cell, their impedance response usually displays a large (several kΩ cm^2) arc due to the charge transfer reaction of the polysulfide species on the glassy carbon surface. The characteristic peak frequency of this arc is in the range of 1–20 Hz (Fig. 5e, black spectrum).

The Mg symmetrical cell was assembled using Mg electrodes that were pre-passivated for 1 hour by soaking the electrode discs in a vial containing the Mg electrolyte. The electrodes were washed with dioxolane solvent before being used for cell assembly with a polysulfide-containing electrolyte without Mg salt. If the passivated electrodes exhibited neither ionic nor electronic conductivity, the resulting impedance spectrum with polysulfide addition would be blocking in nature and would not display any of the previously described characteristics. However, the measured impedance spectrum matched the expected response of a single arc of several kΩ cm^2 at 1–20 Hz (Fig. 5e, grey spectrum). Additionally, the evolution of the impedance spectra was monitored for several hours. The polysulfide-containing Mg||Mg cell showed very stable impedance spectra with minimal variation (Fig. 5f, yellow lines), in stark contrast to the significant impedance growth previously discussed for a symmetrical Mg cell at OCV (Fig. 5f, grey lines).

We additionally repeated this experiment using an *operando* setup. Instead of pre-passivating the Mg electrodes, washing them and then using polysulfide containing electrolyte for cell assembly, we conducted the experiment without any disturbance to the interfaces. For this experiment, the cell shown in Fig. 1c and d was used in a two-electrode configuration. The evolution of the impedance spectra was monitored for one hour at open circuit voltage to allow the electrodes to passivate. During this time, the resistance of the measured arc increased from approximately 180 kΩ cm^2 (250 mHz) to 400 kΩ cm^2 (125 mHz), see Fig. 5g. After one hour, 0.5 M Li_2S_8 solution was added to the cell, diluting the polysulfide solution to 0.1 M. Upon this *operando* polysulfide addition, the impedance response changed drastically, decreasing to approximately 2.5 kΩ cm^2 with a peak frequency between 3 Hz and 12 Hz. Fig. 5h shows the measured data for 1 h after polysulfide addition. Apart from the significant 100-fold decrease in impedance, the spectra also showed much better stability. Overall, the *operando* experiment supports the previously conducted tests and the hypothesis of significant electronic conductivity of the Mg surface passivation layer.

 This journal is © The Royal Society of Chemistry 2026

Discussion of the effect of interphase properties on Mg anode operation

With this new knowledge, we need to revisit all previous experiments and discuss how the electronic conductivity of the passive layer affects the explanations of the observed phenomena. The behavior of the Mg electrode was shown to differ significantly from that of the lithium metal anode. We attribute this primarily to the inherently poor conductivity of Mg ions in solids, as exemplified by the scarcity of solid-state Mg-ion conductors. Consequently, we exclude the possibility that the Mg passivation layer functions as a Solid Electrolyte Interphase (SEI). By definition, an SEI is characterized by high ionic conductivity and negligible electronic conductivity. In contrast, the passive film observed on Mg exhibits poor ionic conductivity and significant electronic conductivity. Electrochemical impedance spectroscopy and morphological analysis were used to quantify these transport parameters, as shown below.

Continuous surface passivation under OCV conditions and the formation of a porous passivation layer can occur only when both electrons and Mg ions cross the passivation layer. The measured thickness of the porous passivation layer (Fig. 3b) allows estimation of the capacity associated with this corrosion process. This capacity is directly related to the resistance from Mg ion migration in the compact passivation film, as this migration is more difficult than electron tunneling in the studied system and thus determines the overall corrosion rate. Assuming 50% porosity and a 300 nm thickness of MgO formed over 72 hours of reaction time yields a current of 0.8 μA. With an estimated voltage difference of 1 V, the resistance for Mg ion migration through the compact passivation film is in the MΩ cm^2 range.

To measure the electronic resistance of the layer, the polysulfide experiments described above can be used. In these experiments, the resistance difference between the GC||GC cell and the Mg||Mg cell was 4 kΩ cm^2 (Fig. 5e). This value can be attributed to the electronic resistance of the layer. However, it is important to consider that (i) polysulfides disproportionate, which can shift the resistance of the arc back and forth,[17] and (ii) the ionic conductivity of the layer is not infinitely large, so some corrosion occurs, reducing polysulfides and increasing the arc resistance in Mg||Mg cells. Therefore, the conclusion is that the resistance for electron tunneling through the layer at open-circuit voltage is at most a few kΩ cm^2. Notably, according to the Simmons model,[16] this value decreases according to a cubic law when the cell is under bias, so the resistance due to electron passage during galvanostatic measurements is considerably lower.

Using these parameter values, we first examine the OCV response of the Mg metal anode. As shown in Fig. 2, the resistance values during the first 20 hours of measurement increase from 40 to 400 kΩ cm^2, while the capacitance remains relatively stable at approximately 17 μF cm^{-2}. As hypothesized, the resistance drift could result from a decrease in passive layer conductivity, changes in active reaction sites, or both. We assume that at OCV, the ionic and electronic resistances are in parallel (since either can contribute to the electrochemical response) and are followed in series by the charge transfer reaction coupled with double-layer capacitance. Because the passive layer resistances are in parallel, the resulting resistance will be less than the smaller electronic resistance. Therefore, the OCV EIS spectra are expected to show a contribution from passive layer resistance of less than a few kΩ cm^2.

Since this calculated value is much smaller than the measured impedance (Fig. 2), it is most likely that, among the three possible explanations for the phenomenon, only the charge transfer reaction is being observed. We believe the measured impedance increase results from changes in the availability of suitable reaction sites on the passive layer surface, which are affected by passive layer reordering. We propose that the effect of changes in suitable reaction sites is correlated with the multi-step nature of Mg reactions, which include surface-adsorbed species, as this adsorption process can be highly specific to the exact surface chemistry.[18]

Let us now consider the data collected when the cell is under bias. As discussed, the asymmetry of the processes, poor ionic conductivity, and good electronic conductivity suggest that stripping occurs through the breakage of the passive layer, exposure of bare Mg, and reactions at those open sites. This implies that (i) the impedance measured on the electrode during stripping after activation reflects the charge transfer reaction on an (as yet unknown) percentage of the Mg electrode, where bare Mg was exposed during activation, and (ii) before activation, we should observe very large overpotentials (1 MΩ cm^2 times the current density). In our experiments, this would result in 300 V to 1 kV of overpotential, depending on the applied current. However, this value is never actually observed in measurements, not even in cases where we initially assumed the electrode was non-activated (before "activation" in galvanostatic experiments, Fig. 4a). With this additional knowledge, we presume that the largest activation occurs at very short times upon applying a current bias, when we do not detect it with the employed measurement settings. The second drop is likely an additional, second-step activation process. At this point, we do not have a solid explanation for why the second activation occurs and why the time at which it occurs is nearly constant.

For the electrode undergoing stripping, we assume that the activated surface area directly correlates with the current responsible for activation, while the measured charge transfer reaction resistance is directly associated with the size of the open surface area. Thus, higher currents activate more of the electrode and more significantly reduce the charge transfer resistance. This effect explains why we do not observe a clear correlation between current density and overpotential values. Since the exact degree of surface activation is unknown, it is also difficult to reconstruct the voltage–current characteristic, so we do not know the specific effect that current density has on the charge transfer reaction resistance. Nevertheless, we know that the total charge transfer reaction resistance contributions for Mg oxidation are relatively small, since the total resistance values calculated from the current and overpotential after the second activation step vary between approximately 30 and 300 Ω cm^2 (for 10 mA cm^{-2} and 0.3 mA cm^{-2}, respectively; assuming the Mg reference electrode is stable).

On the plated side, the situation is fundamentally different. Due to the electronic conductivity of the passive layer, we assume that after initial deposition at isolated preferential reaction sites (where the reaction occurs during OCV), the plating reaction rapidly spreads over most of the electrode surface. The already deposited atoms serve as low-energy anchors for further metal deposition. Unlike stripping, which after activation is largely determined by the reaction mechanism, the rate of plating depends on both electron conduction through the passive layer and the deposition reaction itself. Thus, the corresponding impedance response consists of arcs representing the electronic resistance of the passive layer and the charge transfer reaction. Both decrease when current bias is applied – the former drops with the cube of the current according to the Simmons model, while the latter decreases according to the voltage–current characteristic, which depends on the actual mechanism, currently unknown. However, some predictions about the current–overvoltage characteristic can still be made based on the general behavior of multistep electrochemical reactions involving multivalent ions, as discussed below. A further complication in this system is that the response is inherently connected to changes in morphology, which, as shown, is directly affected by the current density (Fig. 4g–j). Nevertheless, we estimated the surface difference between the lower and higher currents used and found minimal differences in size.

Our data for the specific electrolyte and currents tested show that the overpotentials remain constant at lower currents and are slightly higher at the highest current tested. We assume this difference may result from the formation of concentration gradients and mass transport limitations at 10 mA cm^{-2}. Because the electrode's total surface area is minimally affected by the morphologically different deposits and there is no clear variation in overpotential during the experiment when deposits are made, we reject the hypothesis that the overpotential variation (or lack thereof) is geometrical in origin. Furthermore, if electronic resistance was the main bottleneck, we would expect a clear change in overpotentials with changes in current density – a tenfold increase in current should correspond to a thousandfold increase in resistance.

We therefore believe it is more likely that the charge transfer reaction contribution controls the operation. The minimal overpotential variation between 0.3 mA cm^{-2} and 3 mA cm^{-2} (Fig. 4b) can be explained by a current–voltage curve with very little change in current up to a certain overpotential, followed by activation of the reaction (approximated by an exponential relationship) at higher overvoltages, which is characteristic of multistep reactions (see examples in ref. 18 and 19). This also suggests a significantly different order of magnitude for charge transfer resistance between stripping and plating, which, apart from the inherent asymmetry of oxidation *versus* reduction, is assumed to be affected by the fact that one occurs on bare Mg, while the other takes place on top of the passive film.

The impedance of both oxidized and reduced Mg electrodes is therefore controlled by charge transfer reactions, but there is an inherent difference in where these reactions occur. During stripping, the ionically non-conductive passive layer must break to expose bare Mg. Not all of the electrode is active, yet we typically observe low associated resistances. In contrast, the mechanism differs due to the electronic conductivity of the interphase, as deposition can occur on top of the passive layer. In this case, the entire surface area of the electrode is inherently active, but the resistances are significantly larger (approximately tenfold, as estimated from overpotentials while disregarding the non-linearity of the current–voltage curve). We assume this may be because the reduction reaction occurs on the passive film, while oxidation occurs on bare Mg.

Conclusions

This work elucidates the complex structure and transport properties of the interphase formed on magnesium metal in chloride-based electrolytes. Contrary to the classical Solid Electrolyte Interphase (SEI) model observed in lithium batteries—which relies on high ionic conductivity and electronic insulation—our findings show that the interphase between magnesium and electrolyte behaves as a relatively good electronic conductor and very poor conductor for magnesium ions.

We identified a dual-layer structure comprising a thin (~7–10 nm) compact inner film and a thicker (up to several hundred nanometers) porous outer layer that facilitates liquid-phase transport of Mg^{2+} ions. This unique architecture creates a fundamental asymmetry in the anode's operation. During stripping, the ionically insulating nature of the compact layer forces the physical rupture of the film to expose bare magnesium. Conversely, plating does not require film breakage; instead, the electronic conductivity of the passivation layer allows magnesium reduction to occur on top of the interphase, likely facilitated by electron tunneling. These results indicate that the performance of magnesium anodes is governed by charge transfer reactions that are largely dictated by the specific properties of this passive film. Additionally, it is important to recognize that reaction losses are closely linked to the properties of the interphase. On the stripped side, electrode performance is limited by the degree of electrode activation, while on the plated side, it is determined by the specific reactivity of the surface sites where the charge transfer reaction occurs. The finding that the interphase is electronically conductive challenges the applicability of traditional SEI engineering strategies for magnesium batteries. Rather than solely focusing on ionic transport, future electrolyte and interface designs must account for the electronic leakage across the passivation layer and the dynamics of film rupture and repair.

Author contributions

SDT: conceptualization, data curation, formal analysis, funding acquisition, investigation, methodology, supervision, validation, visualization, writing – original draft; JM: conceptualization, methodology; BS: investigation; ČS: investigation; OL: investigation; TŠ: investigation; ET: investigation; ID: investigation; NL: investigation, formal analysis; UK: investigation, formal analysis; GK: investigation, formal analysis; MG: conceptualization, formal analysis, supervision, writing – original draft; RD: funding acquisition, writing – review & editing.

Conflicts of interest

There are no conflicts of interest to declare.

Data availability

Data for this article are available at the Zenodo repository at https://doi.org/10.5281/zenodo.18746519.

This journal is © The Royal Society of Chemistry 2026

Acknowledgements

The authors acknowledge the funding from the Slovenian Research Agency ARIS (core program funding P2-0423). SDT acknowledges financial support by the Slovene Research Agency ARIS with research project Z2-4465 funding. The research was cofunded under the HyBReED project, supported by the European Union – NextGenerationEU.

References

1 J. Long, Y. Liu, Z. He, S. Tan, F. Xiong, H. Xu, W. Wang, G. Zhang, Z. Yang and Q. An, *ACS Nano*, 2024, **18**, 15239–15248.
2 D. Zhang, Y. Wang, Y. Yang, Y. Zhang, Y. Zhao, M. Pan, Y. Sun, S. Chen, X. Liu, J. Wang and Y. NuLi, *Adv. Energy Mater.*, 2023, **13**, 2301795.
3 M. Chen, S. Zhang, X. Ge, Z. Yang, G. Sun, A. Du, J. Zhao, S. Li, J. Xiao, H. Li and G. Cui, *Adv. Mater.*, 2025, **37**, 2418761.
4 Z. Fan, W. Zhao, S. Shi, M. Zhou, J. Li, Y. Liu, Z. Pan and X. Yang, *Angew. Chem., Int. Ed.*, 2025, **64**, e202416582.
5 X. Chai, H. Xie, T.-T. Zhang, Y. Xin, F. Zhang, B. He, H. Xie, L. Yu and H. Tian, *Energy Storage Mater.*, 2024, **70**, 103460.
6 R. Zhang, C. Cui, R. Li, Y. Li, C. Du, Y. Gao, H. Huo, Y. Ma, P. Zuo and G. Yin, *Chem. Eng. J.*, 2021, **426**, 130751.
7 G. Li, K. Chen, M. Lei, T. Wang, M. Hu and C. Li, *Adv. Energy Mater.*, 2024, **14**, 2401507.
8 J. Häcker, T. Rommel, P. Lange, F. Kampmann, J. Remmlinger, Z. Zhao-Karger, K. A. Friedrich and M. Nojabaee, *J. Magnesium Alloys*, 2025, **13**, 2680–2698.
9 R. Attias, B. Dlugatch, M. S. Chae, Y. Goffer and D. Aurbach, *Electrochem. Commun.*, 2021, **124**, 106952.
10 S. Drvarič Talian, J. Bobnar, A. R. Sinigoj, I. Humar and M. Gaberšček, *J. Phys. Chem. C*, 2019, **123**, 27997–28007.
11 S. D. Talian, N. Urbanija and M. Gaberšček, *Solid State Ionics*, 2025, **429**, 116987.
12 S. Drvarič Talian, G. Kapun, J. Moškon, R. Dominko and M. Gaberšček, *Nat. Commun.*, 2025, **16**, 2030.
13 S.-K. Otto, Y. Moryson, T. Krauskopf, K. Peppler, J. Sann, J. Janek and A. Henss, *Chem. Mater.*, 2021, **33**, 859–867.
14 A. Križan, T. Ericson, L. King, Q. Liu, R. Temperton, R. Dominko, O. Vodeb, D. Strmčnik, M. Gaberšček and M. Hahlin, *Phys. Chem. Chem. Phys.*, 2025, **27**, 7456–7466.
15 L. Zhao, M. Feng, C. Wu, L. Guo, Z. Chen, S. Risal, Q. Ai, J. Lou, Z. Fan, Y. Qi and Y. Yao, *Nat. Commun.*, 2025, **16**, 4283.
16 A. Robba, A. Vizintin, J. Bitenc, G. Mali, I. Arčon, M. Kavčič, M. Žitnik, K. Bučar, G. Aquilanti, C. Martineau-Corcos, A. Randon-Vitanova and R. Dominko, *Chem. Mater.*, 2017, **29**, 9555–9564.
17 M. V. Bracamonte, A. Vizintin, G. Kapun, F. Cometto, J. Bitenc, A. Randon-Vitanova, M. Gaberšček and R. Dominko, *J. Power Sources*, 2023, **555**, 232367.
18 T. Pavčnik, J. Šuster, E. Tchernychova, J. Bitenc and R. Dominko, *Batter. Supercaps*, 2026, **9**, e202500265.

19 A. Vizintin, J. Bitenc, A. Kopač Lautar, K. Pirnat, J. Grdadolnik, J. Stare, A. Randon-Vitanova and R. Dominko, *Nat. Commun.*, 2018, **9**, 661.
20 J. G. Simmons, *J. Appl. Phys.*, 1963, **34**, 1793–1803.

 This journal is © The Royal Society of Chemistry 2026